Simulations of breaking wave impacts on a rigid wall at two different scales with a two phase fluid compressible SPH model

P.M. Guilcher(1), *L. Brosset*(2), *N. Couty*(1), *D. Le Touzé*(3)
[1]*HydrOcean*, Nantes, France
[2]*GTT* (Gaztransport & Technigaz), Saint-Rémy-lès-Chevreuse, France
[3]*Ecole Centrale Nantes*, Nantes, France

ABSTRACT

After years of efforts (Deuff, 2007, Oger et al., 2009; Guilcher et al., 2010), *HydrOcean* and *Ecole Centrale Nantes*, supported by *GTT*, succeeded in the development of a SPH software gathering all functionalities for relevant simulations of sloshing impacts on membrane containment systems for LNG carriers.

Based on Riemann solvers, *SPH-Flow* deals with two compressible fluids (liquid and gas) that interact with the impacted structure through a complete coupling. The liquid, the gas and the structure are modelled by different kinds of dedicated particles allowing sharp interfaces. An efficient parallelisation scheme enables to perform calculations with a sufficiently high density of particles to capture adequately the sharp impact pressure pulses.

The development of the bi-fluid version led in a first stage to unstable solutions in the gaseous phase for pressures below the ullage pressure. This difficulty was presented in ISOPE 2010 (see Guilcher et al., 2010) and has been overcome since.

Simulations of a unidirectional breaking wave impacting a rigid wall after propagating along a flume are presented in this paper. The physical phenomena involved in the last stage of the impacts are scrutinized and compared with experimental results from Sloshel project (see Lafeber et al., 2012b). A comparison between calculated results at full scale and at scale 1:6 is proposed. Conclusions about scaling in the context of wave impacts are given.

KEY WORDS: Sloshing, SPH, Liquid Impact, Compressibility, LNG carrier, Speed of sound, Breaking Wave, scaling, ELP, CFD, Bagnold.

INTRODUCTION

Context

Today, experiments at small scale and numerical simulations are to be considered as complementary for the study of sloshing impacts on board LNG carriers but their respective role is very different:

- Any sloshing assessment of a real project relies on sophisticated Sloshing Model Tests (see Gervaise et al., 2009) that numerical simulations are still very far to match in any way. But the model tests results are biased due to local physical phenomena that exist at full scale (phase transition, fluid-structure interaction) but not at model scale or that do not follow Froude similarity (compressibility of both the gas and the liquid phases, surface tension, etc.).
- Numerical simulations, though still very simple, in terms of physics involved, compared to the reality, help understanding these biases and therefore contribute to improve the experimental modelling (better representativeness of sloshing model tests) and to post-process more relevantly the biased model tests results.

For the time being, *GTT* developed a know-how based on the feedback from the LNG carrier fleet in order to derive appropriate statistical scaling factors. At the same time a research work is carried out to define a more direct approach. The support given by *GTT* to *HydrOcean* and *Ecole Centrale Nantes* in order to improve their *SPH-Flow* software in the context of liquid impacts is part of this research work and consistent with this overall vision.

Elementary Loading Processes (ELP)

Scaling impact pressures from sloshing model tests to the full scale of an LNG carrier implies being able to decompose all the loading components for any liquid impact on the walls and evaluate their relative importance at both scales. This question has been addressed by Brosset et al. (2011) by analyzing a single impact of a breaking wave on a wall, thanks to the concept of Elementary Loading Process (ELP) described in detail in Lafeber et al. (2012a).

The loads induced by any breaking wave impact and more generally by any liquid impact on a wall are time and space distributed. These distributions are considered as a combination of only three components:

- ELP1: *Direct impact* due to the discontinuity of velocity imposed by the wall to the liquid particles. This ELP is associated to the liquid compressibility (pressure waves) and the elasticity of the wall (strain waves). It leads to very sharp pressure peaks that are difficult to detect experimentally.
- ELP2: *Building jet*. This is simply the hydrodynamic load associated to the change of momentum imposed by the wall to the flow. It is significant only at the root of the jets building along the wall just after the contact. The pressure signature is a travelling pulse at the root of the jet which can be very sharp in some conditions like Flip-Through impacts.
- ELP3: *Compression/expansion of gas* while escaping or when entrapped. This ELP is associated to the compressibility of the gas.

It is characterized by pressure oscillations, at least when no phase transition is involved (see Ancellin et al., 2012).

Other physical phenomena involved during a liquid impact (e.g. phase transition, fluid-structure interaction and the generation of free surface instabilities like Kelvin-Helmhotz or Rayleigh-Taylor (see Drazin, 2004)) modify the development of these ELPs and therefore influence the resulting load. Nevertheless they do not have their own related ELP.

The most typical combination of ELPs, as determined from many wave impact tests in flumes, was summarized in a simple chart by Lafeber et al. (2012a). All the possible associated physical phenomena are included in the chart. This chart is shown in **Figure 1**.

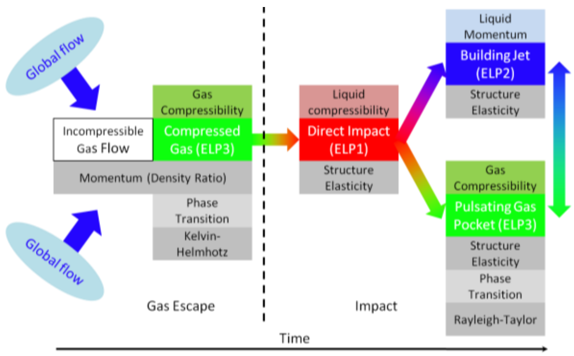

Figure 1 – Impact chart: typical combination of ELPs and associated physical phenomena (from Lafeber et al., 2012a).

Each of these ELPs considered separately follows a different similarity law. The main problem for scaling is therefore due to the interactions between them.

GTT's strategy consists in studying at different scales relevant scenarios staging more and more complex combinations of ELPs and associated physical phenomena. The scenarios are studied either by dedicated experiments (Lafeber et al., 2012b) or semi-analytical developments (Ancellin et al. (2012)) or *numerical simulations* (Braeunig et al., 2009).

Presentation of the paper

Scaling effects are studied through 2D simulations of an air-pocket-type breaking wave impact on a rigid vertical wall at full scale and at scale 1:6. Fluids involved are water and air.

As the compressibility of the gas and of the liquid is taken into account in the model, the three ELPs with their associated physical phenomena are supposed to be present in the simulation. As the wall is assumed as rigid, as there is no thermodynamic model into the code and as, though quite refined, the density of particles proposed in the models is not large enough to simulate adequately the free surface instabilities, the scenario of breaking wave studied in this paper corresponds to the simplified impact chart shown in **Figure 2**.

The simulations were performed with *SPH-Flow* software developed commonly by *HydrOcean* and *Ecole Centrale Nantes*. This software is presented in next section.

This type of wave impact in a flume has been studied experimentally within the Sloshel project, also at these two scales (see Lafeber et al., 2012b). A qualitative comparison between experimental and numerical results is proposed.

The different parts of the time-space distribution of the loads are analysed and compared at both scales through the notion of ELP. Finally the pressures are directly compared at both scales in the different areas of the load distributions where it makes sense.

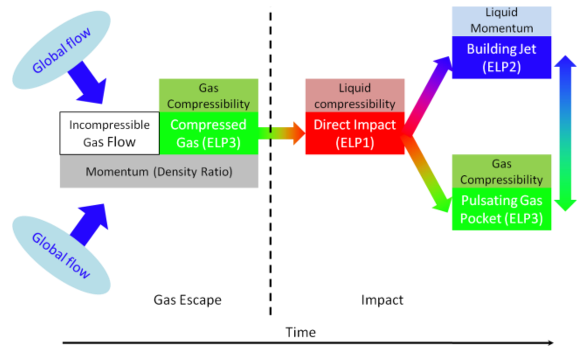

Figure 2 – Simplified impact chart corresponding to the simulations of breaking waves as performed by *SPH-Flow*.

SPH-FLOW SOFTWARE

SPH-Flow is a multi-purpose, multi-physics CFD Software. It has been developed by ECN and *HydrOcean* through several PhD works (see Doring, Oger, Deuff, Guilcher, Grenier, de Leffe). The solver was first developed for fluid flow simulations dedicated to complex non-linear free surface problems. *SPH-Flow* has now been extended to multi-fluid, multi-structure, fluid/structure interaction and viscous flows. It relies on state-of-art meshless algorithms, such as Riemann solver upwinding, MUSCL reconstruction and gradient renormalization for increasing the order of the formulation.

Lagrangian meshless methods bring significant advantages over classical mesh-based methods for specific applications. The Lagrangian motion of particles enables non-diffusive, thus very sharp, interfaces. It proves to be well adapted for multi-species problems. Complex geometries in free or arbitrary forced motions can also be dealt with, without requiring any remeshing procedures. Compressible formulation enables to take into account all compressibility effects that occur during impacts, either in the liquid or in the gas.

Multi-fluid formulation

The SPH model selected for multi-fluid applications is based on an interface treatment first proposed by Leduc (Leduc et al., 2009) and adapted in *SPH-Flow* (Guilcher et al., 2010), enabling very small density ratios and realistic values for the speeds of sound.

The system of conservation laws corresponds to the isentropic Euler equations and is written in conservative form for each phase:

$$L_{\vec{v}_o}(\Phi) + div\,(F_E(\Phi) - v_o\Phi) = S \tag{1}$$

Φ is the vector of conservative variables, F_E the Eulerian flux matrix and S the source term per unit of volume. The system of equations is written in an arbitrary moving reference frame (Arbitrary-Lagrange-Euler (ALE) description) where v_o denotes the transport velocity field.

To close the system, a generic Tait Equation of State relating pressure to density is used:

$$p = \frac{\rho_0 a_0^2}{\gamma}\left(\left(\frac{\rho}{\rho_0}\right)^{\gamma} - 1\right) \tag{2}$$

ρ_0, a_0 and γ are respectively the nominal density, the nominal speed of sound and the isentropic constant for the considered fluid.

Fluid domain is discretized by a set P of particles. Each particle i has a location x_i, a volume of control w_i and carries its own properties (velocity, pressure, etc.). A weak formulation associated to (1) by use of SPH spatial derivative operators leads to the following scheme for Euler equations:

$$\frac{d}{dt}(w_i\Phi_i) + w_i \sum_{j\in P} w_j 2G\left(\Phi_i,\Phi_j,n_{ij}\right)B_{ij}\cdot\nabla W_{ij} = w_i S_i \qquad (3)$$

Upwind numerical flux G is given either by exact or approximate Riemann solvers in the moving framework. Extension to second order with MUSCL algorithm is performed with linear reconstruction on pressure and velocity. The term B_{ij} stands for the symetrized renormalization matrix (Vila, 2005).

Ordinary Differential Equations are marched in time with classical 4th order Runge-Kutta scheme, or 3rd order Strong Stability Preserving Runge-Kutta scheme. Time step is restricted by a CFL-like condition on acoustic waves.

A specific treatment is applied at the interface between two fluids. Mono-fluid Riemann solver is replaced by a multi-fluid linearized approximate Riemann solver. Riemann problem relies on the continuous variables across interface, namely the pressure and the normal velocity, instead of using the conservative variables. Moreover, upwind velocity resulting from the Riemann solver is used together with the ALE framework in order to block mass transfers between the fluids. Thus, Lagrangian form of the ALE formalism is implicitly assumed at the interface.

This multi-fluid model has been intensively validated for 1D compression of a gas column, with comparison to the semi-analytical Bagnold's solution (see Bagnold, 1939 and Guilcher et al., 2010).

Multi-structure formulation

The multi-physical feature of SPH enables to adapt easily the fluid formulation to the modeling of structures, by only a a few changes. The degenerated equation of state $p = c_0^2(\rho - \rho_0)$ is used.

In this condition, the equation of state must respect the Hook condition, linking stress and strain rates in the medium, by imposing c_0 such that $c_0^2 = \frac{E}{\rho_0}$, where E corresponds to the Young modulus of the material.

The main difference between the SPH scheme for fluids and structures relies in the adjunction of a deviatoric part in the stress tensor as $\bar{\bar{\sigma}} = -p\bar{\bar{I}} + \bar{\bar{S}}$ based here on the Jaumann rate S (Shintate, 2004).

Validations were performed for multi-structure problems. For example, the compression of a Mark III containment system was studied and compared successfully to a Finite Element reference solution (Oger et al, 2009).

Fluid-Structure Interaction (FSI)

SPH model previously discussed for fluids and structures has been adapted to fluid/structure interaction problems through a PhD Thesis (*GTT/ECN*) (Deuff, 2007). It relies on the respect of kinematic and dynamic conditions at the fluid/structure interface.

As this important functionality has not been used for the study presented here, the reader is invited to look at previous publications (Oger et al. (2009) and Guilcher et al. (2010)) for more details.

Tensile Instability

SPH method is subjected to the so-called Tensile Instability (see Swegle et al., 1995), which develops when a continuum such as fluid or structure is under tension. This numerical instability leads to unphysical fractures of the material, with apparition of void cavities. The problem is well known for structure applications. It appeared also in the gas during our previous attempts of wave breaking impacts simulations (see Guilcher, 2010). **Figure 3** shows a void cavity generated by Tensile Instability at the tip of a wave crest during these previous SPH simulations. Calculations crashed just afterwards.

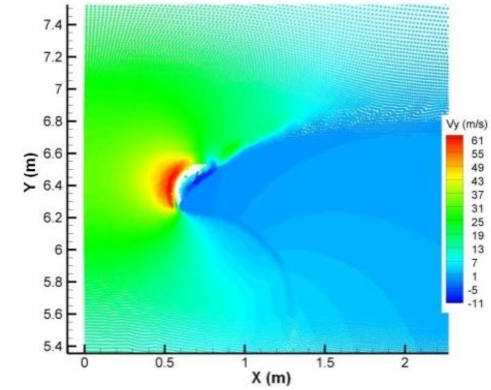

Figure 3 – SPH Simulation of a wave crest approaching a wall while breaking. Apparition of void cavities due to Tensile Instability. From Guilcher et al. (2010).

A specific procedure was developed to solve the problem, while preserving the main characteristics of the SPH method, in particular the conservation properties of the discrete scheme.

Parallelization

SPH-Flow solver is parallelized to reduce the return time of a computation by use of cpu resources available on clusters. This distributed memory parallelization relies on a domain decomposition: the computational domain is divided in as many sub-domains as allocated processes. The communications between processes are achieved through the MPI library.

The speedup of the parallelized solver was evaluated through a parametric study both on number of particles and number of processes (see **Figure 4**). Classically, the speedup increases with the number of processes, up to a returning point. Then limitations due to communication latencies decrease the efficiency. For each size of problem (number of particles) there is an optimal number of processes to adopt.

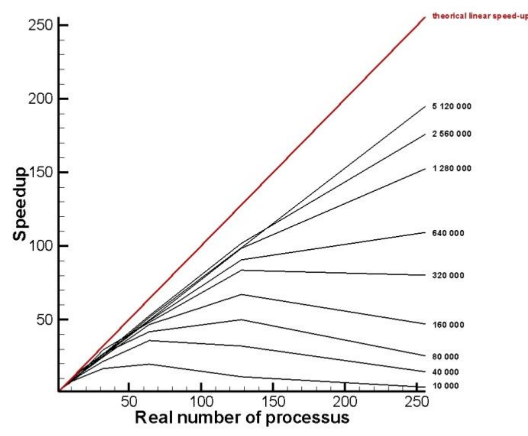

Figure 4 - Speedup of renormalized formulations using Riemann solver on a dam break test case.

Work is on going to improve the performances for large number of processes (several thousands) by modifying parallel algorithms and developing a hybrid OpenMP-MPI version.

CALCULATION CASES

2D simulations with *SPH-Flow* of a selected breaking wave impacting a rigid vertical wall are presented. Liquid and gas involved are respectively water and air in the reference calculation.

Wave generation by FSID

Generation of the wave is obtained by FSID, a potential code based on a succession of transformal mappings and a desingularized technique, developed by Scolan (see Scolan, 2010). The wave is generated in a large rectangular tank assuming an arbitrary initial shape of the free surface and a given bathymetry just in front of the wall. The initial wave shape and the shape of the tank bottom in front of the wall are parametrically fitted in order to obtain the desired shape of the impacting wave. Only the liquid is taken into account in FSID model.

FSID is well suited for simulations of slosh type of impacts including the limit case of flip-throughs, as described in Scolan (2010). But it cannot introduce a new contact area with the wall as it occurs with a crest impact. Therefore, FSID is used in our study to select a wave shape and to initialize SPH calculations at a given instant before the impact.

For the wave selected in this study, the only initial requirement was to obtain a breaking wave impact with a large air-pocket and a maximum crest velocity in the order of magnitude of 10 m/s, considering a water depth at rest of 4 m. The wave was requested also to match qualitatively the wave shapes obtained experimentally in a flume by a wave maker using a focusing method, like those obtained during full scale campaigns of Sloshel (see Kaminski et al., 2011).

The selected wave, as simulated by FSID at different time steps is represented in **Figure 5** (left). It was obtained with a 20 m x 12 m rectangular tank. The tank bottom is a quarter of ellipse, the two main half dimensions of which are 18 m x 2.8 m.

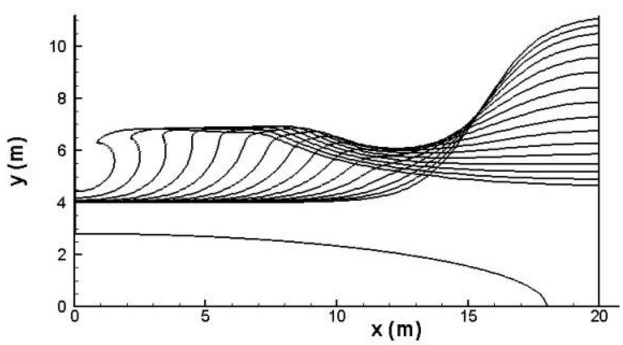

Figure 5 – Shapes of the selected wave at different instants, as simulated by FSID.

Initialization of *SPH-Flow* calculations

SPH-Flow calculation is performed in the same rectangular tank as for FSID calculation but starting at a later instant t_0. An initial distribution of liquid and gas particles is prepared, complying with the shape of the free surface as calculated by FSID at t_0. Velocities and pressures for the liquid particles are imposed according to FSID data. The gas particles start from rest with a hydrostatic distribution of pressure.

Initial time t_0 is chosen as late as possible, as long as the gas flow can still be considered as incompressible and there is enough time before impact for the gas flow to be well established.

Figure 6 shows the shape of the selected wave and the velocity modulus at initial time calculation for *SPH-Flow*.

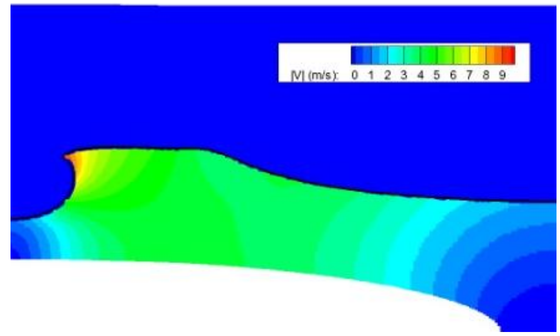

Figure 6 – *SPH-Flow* calculation at scale 1 (case 1) – Velocity modulus at initial time on the complete domain.

Calculations cases

Five calculations have been performed in order to simulate the selected wave:

- Case 1 is performed at full scale with water and air;
- Case 2 is made at scale 1:6 by down-scaling FSID initial flow conditions with a Froude similarity, with water and air;
- Case 3 is a restart of scale 1:6 calculation (Case 2) just before the crest impact, after up-scaling to scale 1 the flow data, with water and air;
- Case 4 is identical to Case 3 but fixing a *scaled speed of sound* in the liquid at 3674 m/s;
- Case 5 is identical to Case 3 but fixing the speed of sound in the liquid at 343 m/s.

Obviously Case 4 and Case 5 are performed with virtual liquids that do not exist in reality. This is one of the advantages brought by numerical simulations. This is intended to help explaining some discrepancies between Case 1 and Case 2 after up-scaling the results of Case 2 by a Froude similarity. **Table 1** summarizes the different calculation cases and the main properties of liquid and gas for each of them.

Table 1 – summary of the calculation cases and main characteristics of liquids and gases involved.

		Liquid**			**Gas****		
Case	**Scale**	**γ**	**ρ_0**	**C_0(m/s)**	**γ**	**ρ_0**	**C_0(m/s)**
1	1	7	1000	1500	1.4	1.2	343
2	1:6	7	1000	1500	1.4	1.2	343
3*	1	7	1000	1500	1.4	1.2	343
4*	1	7	1000	3674	1.4	1.2	343
5*	1	7	1000	343	1.4	1.2	343

**restart calculation from data obtained in case 2 at scale 1:6 just before the first contact of the crest.*
***γ is the isentropic constant, ρ_0 the density and C_0 the speed of sound.*

Calculation models

The particle distributions for the five calculation cases are derived from the same initial distribution at scale 1 for Case 1 and relevantly scaled according to the calculation case. A distribution of 600,000 particles is adopted with a high refinement in the crest region, where the highest pressures are expected. Distance between particles in this area at initial time is about 5 mm at full scale. This refinement is more than sufficient to determine accurately the pressure within gas pockets but this density of particles turns out to be still insufficient to capture accurately the maximum pressure at the crest for all calculation cases except Case 5. Nevertheless, it is believed to be sufficient to derive all conclusions presented.

Equation of state for both the gas and the liquid is chosen as the Tait equation as described in Eq. (2) (see **Table 1** for the characteristics of liquids and gases for the different calculation cases).

A unique reference system (O, x, y) is used throughout this paper corresponding to the full scale case. Its origin O is located at the intersection of the vertical wall and the flat bottom. Horizontal axis x points towards the liquid and vertical axis y points upwards. Time is denoted t, starting from t_0.

Pressure P and vertical velocity V_y time histories are given at points on the wall located every 10 mm from y = 4.5 m to y = 7.5 m, almost enabling a continuum of data. These parameters are presented either as surfaces in the plane (y, t) (P(y, t) and Vy(y, t)) or as time histories at selected given locations y_i. The selected locations y_i correspond most of the time at the location of the maximum pressure or any location within the range covered by the entrapped gas pocket. When pressure or velocity 3D-surfaces are presented, the same two different viewing projections enabling a relevant analyze of the results are adopted for all calculations. First projection, referred to as View 1, corresponds to a view of the surface from large values of y and large values of t. Second projection, referred to as View 2, corresponds to a view from low values of y and low values of t (see for instance **Figure 12** displayed under View 1). These surfaces will be referred to as *pressure maps* or *velocity maps* throughout this paper.

After first adjustments, refined calculations have been performed on 64 cores among the 2352 cores of *Caparmor* cluster of *Ifremer* (Fr) on bi-processor cards Intel Xeon quad core 2.8 GHz. Case 1 calculation lasted 19 hours for a physical duration of 0.36 s. Case 2 calculation lasted 32.5 hours for a physical duration of 0.102 s.

Warning: Unless especially mentioned, comparisons between results at both scales are always done at full scale after Froude-scaling scale 1:6 results. For the sake of clarity, *results description related to Froude-scaled results from scale 1:6 are written in* ***Bold-Italic*** *characters without mentioning Froude-scaling. In that case, even reference to full scale results for comparison may sometimes be omitted when obvious.*

COMPARISON WITH REAL WAVES IN A FLUME

Sloshel project consisted in wave impact tests in flume tanks (see Kaminski et al., 2011). The impacted wall in each tank was instrumented with numerous pressure sensors in the area of the impacts, sampling at 50 kHz. High speed cameras were located close to the wall in order to capture the shape of the waves just before and during the impacts. They recorded at 5 kHz and were synchronized with the data acquisition system.

The two last Sloshel campaigns were performed in different flumes at respectively scale 1/6.14 and scale 1, trying to keep all the main dimensions accordingly scaled. The waves were generated by piston-type wave makers at the end of each flume by a focusing technique. All water depths studied were around 4 m at full scale and accordingly scaled at scale 1/6.14. One of the objectives of the project was to generate Froude-similar couples of breaking waves, **before** an impact, in order to enable relevant comparisons of measured impact loads at both scales.

This objective turned out to be very challenging for two main reasons:

- a lack of accuracy on the water depth measurement due to the presence of low frequency sloshing modes, mainly at full scale in the outdoor flume. This accuracy proved to be necessary as, otherwise, a magnified uncertainty was induced on the point location where the wave trains were supposed to focus (focal point);
- a lack of accuracy of the full-scale-test piston course when requested to follow the Froude-scaled steering signals from the scale 1/6.14 tests. This lack of accuracy was corrected successfully by introducing transfer functions to the steering signal, adjusted in order wave elevations measured at scaled locations matched after relevant Froude-scaling.

Finally, two wave couples were considered as sufficiently Froude-similar before impact for a relevant comparison of pressures at both scales. This comparison is studied in Lafeber et al. (2012b). Among these two couples, couple with test M62 at full scale and test L121 at scale 1/6.14 is the one that matches the best our couple of calculated waves (Case 1 and Case 2).

The choice of the calculated wave at full scale was made already three years ago (see Oger et al., 2009) and the modelization has been improving continuously since. Therefore, the real waves and the calculated waves have no reason to match at any scale. For instance the gas pocket is much larger for the calculated wave, the crest is more plunging before the impact in the experiments, the wall was covered by Mark III corrugated membrane at both scales during the tests whereas it was smooth for the calculations. Nevertheless, it is believed that a qualitative comparison of the scaling effects when calculated, on the one hand, and when tested, on the other hand, is relevant.

Figure 7 and **Figure 8** show the Sloshel wave shapes respectively at scale 1 and at scale 1/6.14 just before and just after the impact.

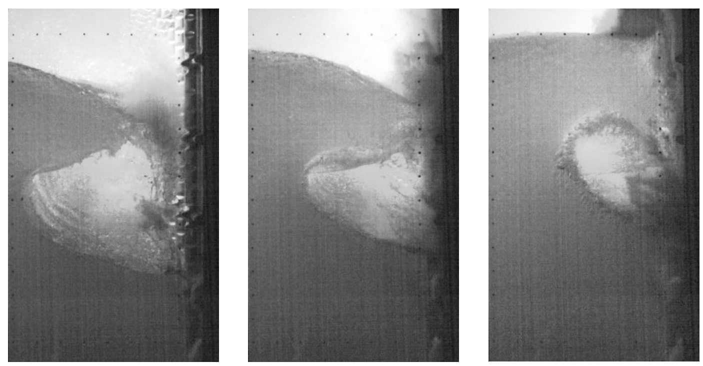

τ_1 τ_2 τ_3

Figure 7 - Wave shape in front of the test wall for Sloshel full scale test M62 with corrugated wall, at three instants τ_1, τ_2, τ_3.

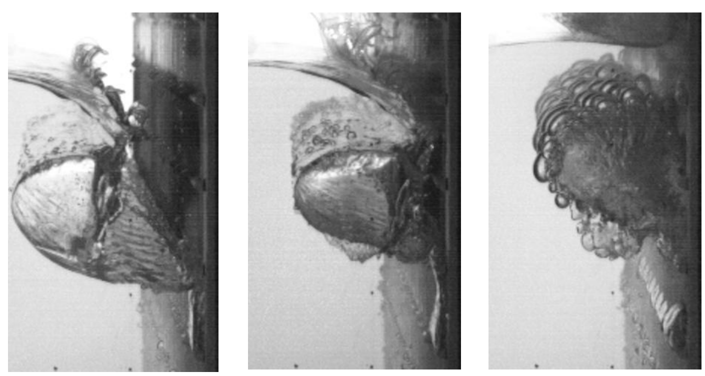

τ'_1 τ'_2 τ'_3

Figure 8 – Wave shape in front of the test wall for Sloshel large scale test L121 with corrugated wall cover, at Froude-scaled instants $(\tau'_i=\tau_i/\sqrt{6.14})_{i=1,3}$.

Figure 9 shows the pressure measurements at both scales, at the pressure sensor having recorded the maximum pressure and at a pressure sensor which remained within the gas pocket during the whole impact duration. Only these two measurements are given as they were not much affected by the presence of the corrugations on the wall. Therefore a fair qualitative comparison with calculated equivalent pressures is relevant.

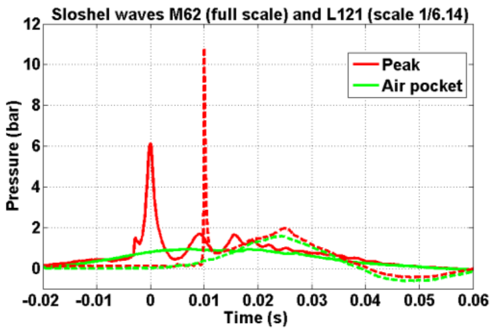

Figure 9 – Measured pressure time histories for Sloshel tests M62 (full scale, continuous lines) and L121 (scale 1/6.14, dotted lines) at sensor giving the max pressure (red) and at a sensor within the gas pocket (green). Time shift between M62 and L121 is arbitrary.
Results of test L121 are Froude-scaled.

These three last figures will be taken as reference when presenting calculated flows and loads at both scales in next sections.

Conclusions in Lafeber et al. (2012b) about the comparison of experimental results at both scales are summarized as follows:

1. The two same types of free surface instabilities develop at both scales but not exactly in the same way:
   - Kelvin-Helmholtz instability (see Drazin et al., 2004) is generated by the strong flow of escaping gas in front of the crest. It leads to a spray of droplets around the crest at scale 1 and to sort-of-liquid strings in the same area at scale 1/6.14. This difference might be due to unscaled surface tensions. This instability is expected to be one of the main reasons for the extreme variability of impact pressure measurements.
   - Rayleigh-Taylor instability (see Drazin et al., 2004) develops behind the free surface of the gas pockets, generating a flow of air through the surface. The typical mushroom shapes are more developed at smaller scale (see **Figure 8**, L121 at τ'_3 compared to M62 at τ_3). This instability is expected to contribute damping the oscillations of the pocket.
2. The point of highest pressure at the crest level (difficult to talk about first contact, considering the spray), is located at a ***higher location*** (see warning in previous section) and ***is delayed*** at scale 1/6.14 compared to full scale. Indeed, the ***crest trajectory*** is slightly deviated upwards at scale 1/6.14, due to a ***stronger flow*** of gas at smaller scale.
3. In these conditions, trying to define a deterministic scaling factor for the maximum pressure does not make sense.
4. Maximum pressures and oscillation periods within the entrapped gas pocket at both scales scale according to Bagnold's model (see Bagnold, 1939). The slight deviation of the crest at smaller scale does not influence significantly this result.

The first point (mentioned in the impact chart of **Figure 1**) is not addressed for the time being in our simulations (not mentioned in the simplified chart of **Figure 2**) as the density of particles is still too low to capture the free surface instabilities adequately. This point is one of the next challenges for numerical simulations of liquid impacts.

The two next sections show that the numerical simulations give exactly the same trends as the experiments for all the other points as far as scaling is concerned.

QUALITATIVE ANALYSIS AT BOTH SCALES

Quantitative comparisons between both scales will be made in last section. A qualitative analysis is first necessary to understand what can be directly compared and what cannot. Qualitative comparisons are made between calculated results at both scales and between simulations and experiments.

Overview

At both scales, both numerically and experimentally, there are three main phases in a breaking wave impact, which are recalled below in a very general way:

1. During the approach of the wave, the gas tries to escape from the entrapment. As it was seen with the experimental results, this leads to a strong gas flow in between the wall and the crest. Time when the vertical gas velocity V_y is maximal is denoted t_1 at full scale and t'_1 at scale 1:6.
2. The gas flow stops at time for which the liquid first touches the wall. At this time, there is a discontinuity of velocity between particles of liquid at the tip of the crest and the wall, which theoretically should lead to a very sharp pressure peak, ELP1-type, the amplitude of which is related to the impact velocity and to the compressibility of the liquid. Time when the maximum pressure is reached is denoted t_2 at full scale and t'_2 at scale 1:6. Just after this contact, the liquid in the crest splits in two main flows: one is going upwards with turns of the velocities above the contact point; the other is going downward with turns of the velocities below the contact point. Both flows feed respectively a vertical upward jet and a vertical downward jet along the wall. When these turns are sharp enough and lead to significant change of the local liquid momentum, high pressures appear at the root of the building jets. The magnitude of the pressure depends on the initial crest velocity, the incidence of the liquid velocities at the tip of the crest with regard to the wall and the shape of the crest. This is ELP2-type load.
3. The entrapped gas pocket volume and its pressure have damped oscillations. Time when the maximum pressure within the pocket is reached is denoted t_3 at full scale and t'_3 at scale 1:6. This is ELP3-type load.

Figure 10 and **Figure 11** show the wave shapes at the three characteristic instants defined above, respectively at full scale and scale 1:6. Left sub-figures are related to instants t_1 and t'_1 when the vertical velocity is maximal in the gas. Therefore, related color-scale refers to vertical velocity. Middle and right subfigures refer to instants when respectively the impact pressure (t_2 and t'_2) and gas pocket pressure (t_3 and t'_3) are maximal. Therefore, related color-scale refers to pressure.

From these two figures, we can make some first observations:

- The ***flow of escaping gas*** is clearly stronger at scale 1:6 than at full scale, due to the gas compressibility bias, as seen when comparing ***vertical velocities*** at $t=t'_1$ and scale 1:6 to vertical velocities at $t=t_1$ and full scale. This is due to ***higher stiffness of the gas*** at scale 1:6.
- This leads to a slight upward deviation of the crest trajectory and a twist of its shape at scale 1:6. Therefore, the crest impacts the wall at a ***higher location*** (y = 6.61 m) at model scale than at full scale (y = 6.47 m).
- ***Time of maximum pressure***, which is very close to time of first contact, is delayed at scale 1:6. Indeed $t'_2 = 0.2021$ s whereas $t_2 = 0.1906$ s.
- The deviation of the crest trajectory and the twist of its shape

upwards lead to different distributions of the initial crest flow upwards and downwards after the first contact at both scales.

- ***Time of maximum pressure into the gas pocket*** is largely earlier at scale 1:6 ($t'_3 = 0.2227$ s) than at scale 1 ($t_3 = 0.2402$ s) despite the initial delay of the impact. This shows indirectly ***highest frequency of the oscillations of the gas pocket*** at scale 1:6.
- ***Maximum pressure within the gas pocket*** is higher at scale 1:6.

These first trends are the same as those observed during Sloshel experiments.

It will be shown later than the tiny flow changes observed between the two scales lead to significant changes on the pressures at wall.

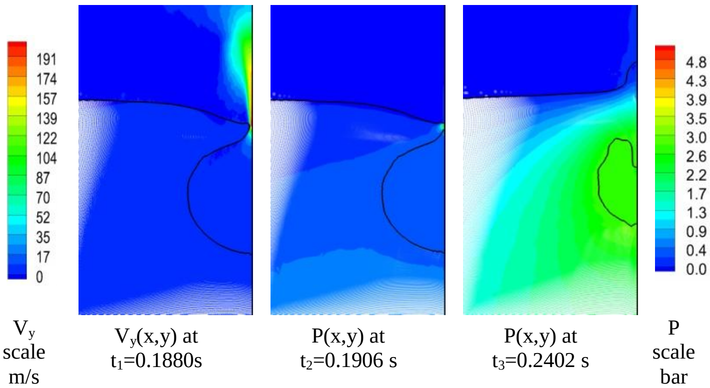

Figure 10 – Wave shapes at full scale for t_1, t_2, t_3 – Case 1.
Left: Colors refer to V_y. t_1 is time of max vertical velocity V_y.
Middle: Colors refer to pressure. t_2 is time of max pressure P.
Right: Colors refer to pressure. t_3 is time of max pressure in gas pocket.

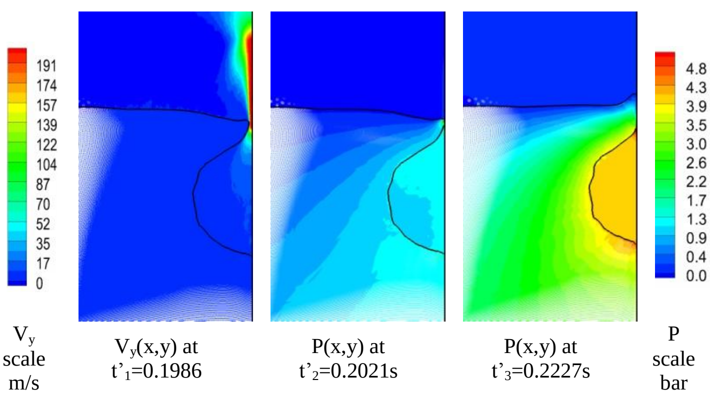

Figure 11 – Wave shapes at scale 1:6 for t'_1, t'_2, t'_3 – Case 2.
Left: Colors refer to V_y. t'_1 is time of max vertical velocity V_y.
Middle: Colors refer to pressure. t'_2 is time of max pressure P.
Right: Colors refer to pressure. t'_3 is time of max pres. in gas pocket.
Case 2 results are Froude scaled.

Figure 12 and **Figure 15** show the pressure maps obtained under View 1 respectively at full scale (Case 1) and at scale 1:6 (Case 2). **Figure 13** and **Figure 16** show the pressure maps obtained under View 2 respectively at full scale (Case 1) and at scale 1:6 (Case 2). Same color and space scales are adopted for these four figures for an easy comparison.

Figure 14 and **Figure 17** show the vertical velocity map obtained under View 1 respectively at full scale (Case 1) and at scale 1:6 (Case 2). Same color and space scales are adopted for these two figures for an easy comparison.

Times t_1, t_2 and t_3 on the one hand and t'_1, t'_2, t'_3 on the other hand are indicated on the maps by intersection lines between the plane section at these given instants and the surfaces, respectively at scale 1 and scale 1:6. These lines define the profile of the parameter (P or V_y) along the wall at the given times.

Different areas can be distinguished on the pressure maps whatever the scale studied. They have been numbered. The areas with their indexes are defined for both scales respectively on **Figure 12** and **Figure 15**. Reference will be made to these areas by means of the indexes throughout the analysis below.

Flow of escaping gas

Whatever the scale, when the wave gets closer to the wall, a flow of escaping gas starts upwards. Comparison between **Figure 14** and **Figure 17** shows clearly that ***the flow*** is stronger at scale 1:6. ***Maximal velocity*** in the gas is 329 m/s at $t'_1 = 0.1986$ s instead of 214 m/s at $t_1 = 0.1880$ s. Thus, ***the delay*** is already 11 ms. Maximal velocities correspond to an actual Mach number of 0.4 at scale 1:6 instead of 0.62 at full scale. Gradient of V_y below the point where the maximum occurs looks also sharp at both scales: velocities are close to zero only ***10 cm*** below this point indicating that the gas flow within the building pocket is quiet outside the channel in between the crest and the wall. Gradient is obviously smoother above this point with still strong gas velocities ***one meter*** above the crest level.

This difference in gas flow strength explains the upward deviation of the crest at scale 1:6 that can be observed on velocity maps by comparing the ***locations of highest V_y near the wall*** at both scales: the ***elevation of this point*** is 6.61 m at scale 1:6 instead of 6.49 m at scale 1.

Pressure in the gas pocket and below

Whatever the scale, at first contact of the liquid with the wall, vertical velocities stop suddenly for all points below the contact point: a gas pocket is now entrapped. All pressure time histories at points on the wall in between the two moving boundaries of the gas pocket are identical. This leads to a perfect cylindrical shape (area 4) on all pressure maps. This is the place of a pure ELP3. The ***duration of a complete period of oscillation*** is much smaller at scale 1:6 than at full scale. On the other hand ***maximum pressure within the pocket*** is larger at scale 1:6: the oscillations of gas pocket pressure do not follow Froude similarity. This will be studied in detail in next section.

The lower boundary of the gas pocket (area 5) looks like a corrugation which is running diagonally on the cylindrical shape of the pocket pressure on the pressure maps. This overpressure is due to the hydrodynamic pressure induced by the run-up of the lower pocket boundary. It can also be distinguished on **Figure 11** (right). This is thus a pure ELP2. The velocity of the trough run-up is given by the slope of the diagonal drawn by the 'corrugation' when looking at pressure maps in plane (y, t). ***This velocity*** is higher at scale 1:6 as ***the compression of the pocket*** is quicker.

Area 6 below the corrugation represents therefore the pressure on the wall in the water below the gas pocket. There is a continuity of pressure between area 4 and area 6, which is also clearly seen on **Figure 10** and **Figure 11** and which ensures a much larger influence of the gas pocket. This had also been observed from Sloshel tests in Bogaert et al. (2010), Brosset et al. (2011) and Lafeber et al. (2012a&b) and called *the remote influence of the gas pocket* by the three authors.

Case 1 at scale 1

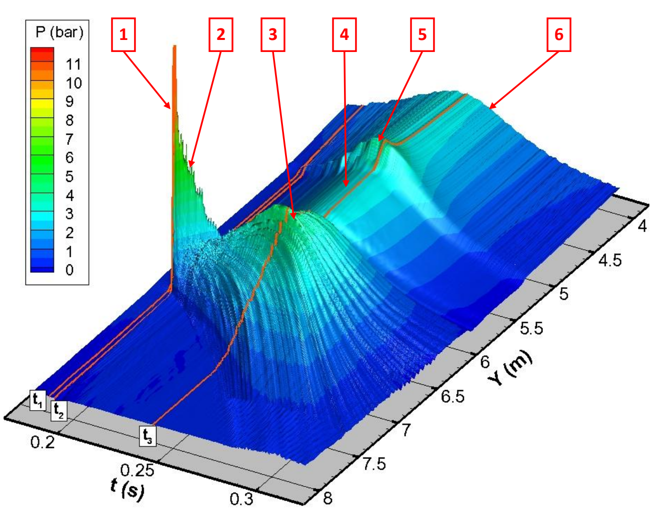

Figure 12 – Time-space distribution of the pressure at wall for full scale simulation (Case 1) – View 1.

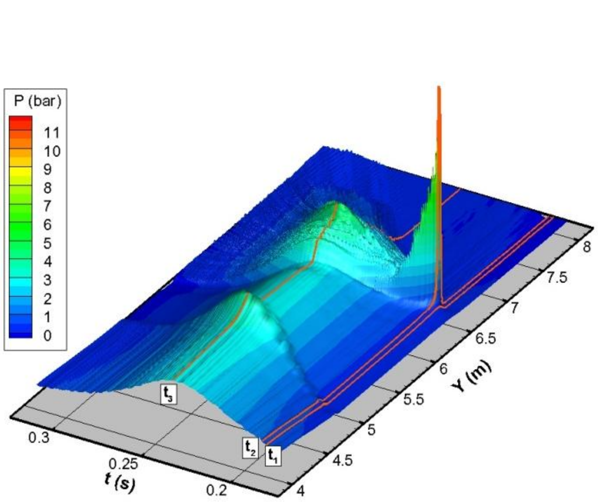

Figure 13 – Time-space distribution of the pressure at wall for full scale simulation (Case 1) – View 2.

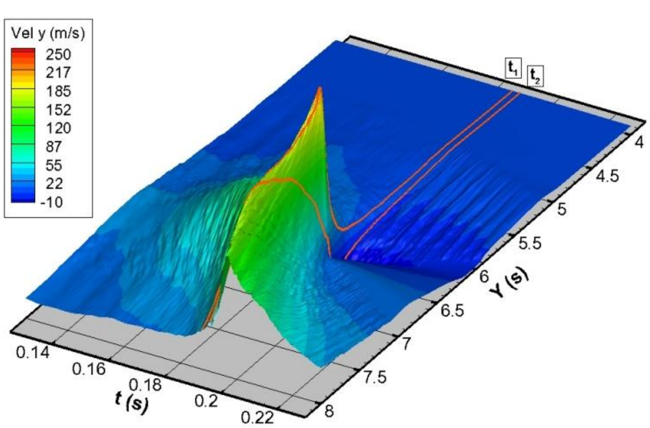

Figure 14 – Time-space distribution of the vertical velocity for the full scale simulation (Case 1) – View 1.

Case 2 at scale 1:6: results are Froude-scaled

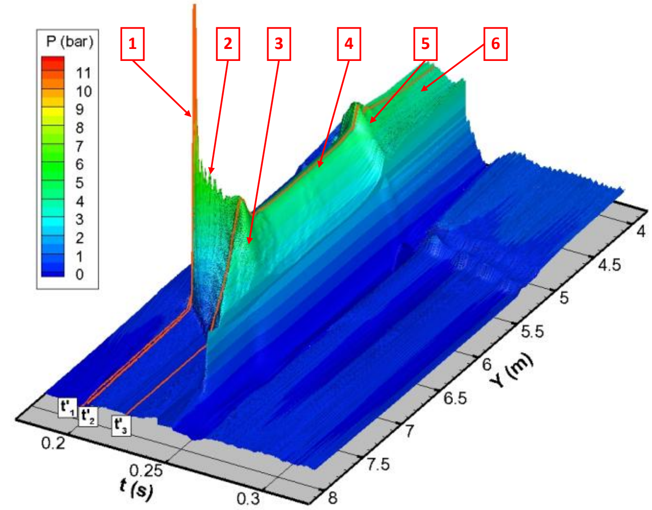

Figure 15 – Time-space distribution of the pressure at wall for simulation at scale 1:6 (Case 2) – View 1.

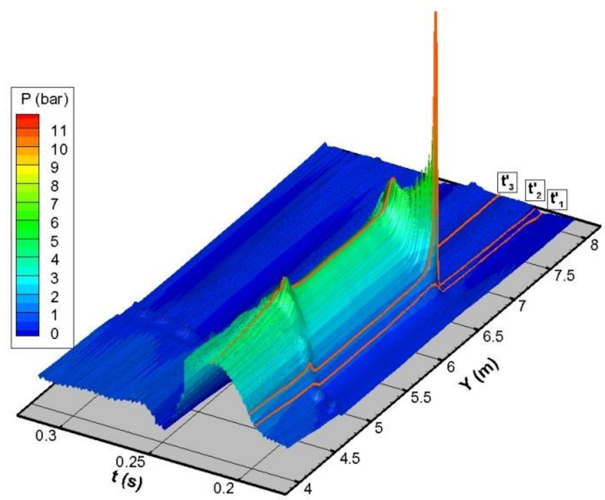

Figure 16 – Time-space distribution of the pressure at wall for simulation at scale 1:6 (Case 2) – View 2.

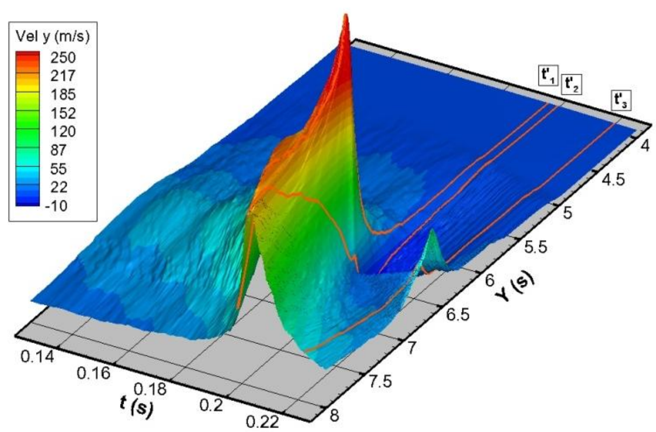

Figure 17 – Time-space distribution of the vertical velocity for the simulation at scale 1:6 (Case 2) – View 1.

Pressure at the wave crest level

Maximum pressure is 13.7 bars at scale 1:6 compared to 10.8 bars at scale 1, hence 27% higher. ***Maximum pressure*** occurs at $t'_2 = 0.2021$ s at scale 1:6 instead of $t_2 = 0.1906$ s at scale 1, hence ***delayed*** at scale 1:6. Moreover, ***this delay*** increased of 0.9 ms since ***the time of maximum vertical velocity***. The maximum pressure is reached very suddenly at both scales because of the discontinuity of normal velocity. The sharp pressure rise at point of maximum pressure corresponds also to a sharp gradient around this point as can be seen when looking at pressure profiles at t_2 and t'_2 respectively on **Figure 13** and **Figure 16**.

At both scales, pressure surfaces in the plane (y, t) appear locally like thin arched blades composed of a sharp peak (area 1) followed by a sharp ridge (area 2) with decreasing pressures (see **Figure 18**) going downward.

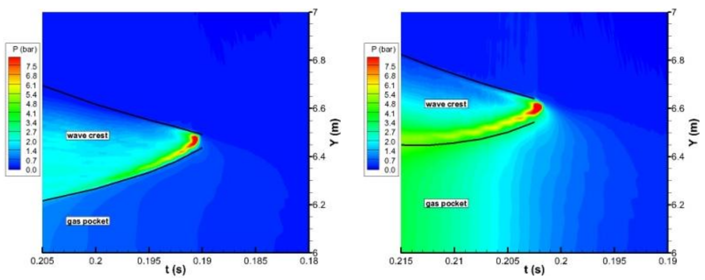

Scale 1 *Scale 1 :6 (Froude-scaled)*

Figure 18 – Pressure at wall versus vertical height y and time t: P(z, t). Boundaries of the crest up and down are drawn in black.

These two areas have been discriminated by referring to different ELPs, respectively ELP1 and ELP2, in wave impact analyses based on Sloshel experiments in Brosset et al. (2011) and in Lafeber et al. (2012a&b). The share and the transition between ELP1 and ELP2 are difficult to sort out precisely from experimental results, mostly because of an always too poor density of pressure sensors. This point will be especially addressed in next section.

At both scales the sharp ridge has a bow shape, oriented downward from area 1 to area 2. These high pressures are located at a liquid point M_{down} at the wall going downwards from the first contact point M_c. The velocity of this point M_{down} can be estimated by the slope of its trajectory in plane (y, t) at both scales from **Figure 18**. It is clearly higher at scale 1 than at scale 1:6, which explains the strong downward flow from the crest that can be observed in **Figure 10** but not in **Figure 11**. Everything appears as though, the more constrained the flow along the wall, because of an initially badly-oriented crest incidence with regard to the wall, the larger the pressure at point where the liquid has to turn abruptly.

If we assumed that there was no compression within the gas pocket, a fixed point on the wall located initially below point M_{down}, hence in the gas, and being met later by M_{down}, hence entering into the liquid, would first feel a sharp peak of pressure (rise and fall) and then a slowly decreasing pressure due to the liquid flow still pushing behind (ELP2). This would be the same kind of pressure signal as observed when studying wedge drop-tests on a flat surface of water. Now, there is a compression of the gas pocket (ELP3) with a remote influence into the crest. Therefore, the two components of the pressure are added: this explains the main shape of area 3. This explains also the pressure gap along the trajectory of point M_{down}, which is the boundary between (area 2 + area 3) and area 4 on the pressure maps (see especially **Figure 13**). Therefore, area 3, is concerned at least by both ELP2 and ELP3.

Whatever the scale, there is also a flow going upwards from the first contact point M_c. The point of highest pressure going upwards from M_c is a liquid point M_{up} within the crest. The pressure at M_{up} vanishes quickly because the liquid flow upwards is not constrained. ***The velocity of M_{up}*** can be measured as the slope of its trajectory in the plane (y, t) in **Figure 18**. It is very similar at both scales.

Figure 19 gathers the pressure histories at points on the wall distributed every 10 mm around the first contact point M_c (green). It allows to better understand the different behavior upwards (red) and downwards (blue) at both scales.

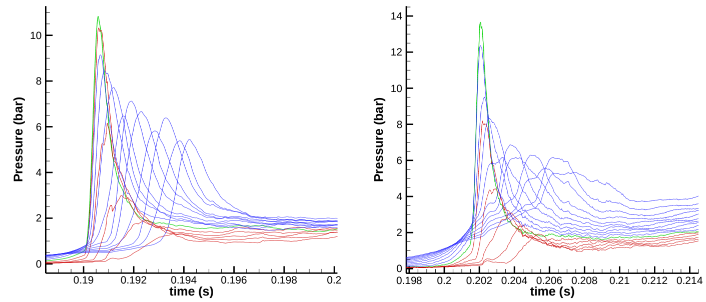

Scale 1 (Case 1) *Scale 1:6 – Froude-scaled (Case 2)*

Figure 19 – Pressure histories at points on the wall distributed in the crest every 10 mm around the first contact point M_c.

At both scales the pressure vanishes upwards in less than 50 mm. It remains strong on a ***larger area downwards*** and ***stronger*** at scale 1:6 than at scale 1.

QUANTITATIVE ANALYSIS AT BOTH SCALES

It has been shown in Braeunig et al. (2009) that, under the assumptions of the simplified impact chart (see **Figure 2**), two liquid impact simulations at two different scales with Froude-scaled inflow conditions give exactly Froude-similar flows and therefore Froude-similar loads (including local pressures) if and only if properties of gases and liquids at both scales are appropriately scaled. This leads finally to have Froude-scaled speeds of sound for the gases and for the liquids. These conditions have been called *Complete Froude Scaling* (CFS) by the authors. If the fluids are real fluids at a given scale, their scaled properties lead to unrealistic fluids at the other scale, unless both scales are close to each other. When fluids are kept the same at both scales, which is the case for our comparison between Case 1 and Case 2, compressibility biases are expected to occur. These conditions have been called *Partial Froude Scaling* (PFS) by the authors.

It has since been shown many times with different codes and with different numerical methods that CFS gave Froude-similar results at different scales for a same code with scaled meshes, even though results from different codes could be very different. This has also been checked many times with *SPH-Flow*. Therefore, considering calculation at scale 1 as reference, let's assume that calculations at scale 1:6 would give exactly Froude-similar pressures if the speed of sound was respectively $343/\sqrt{6} = 140$ m/s in the gas and $1500/\sqrt{6} = 612$ m/s in the liquid at scale 1/6, keeping their initial respective densities. In that case, the ***main characteristics*** P(y, t), V_y(y, t) of the flow would be the same in the different areas described in the previous sub-section at both scales.

For the sake of conciseness only the pressure histories at the points where maximum is reached and the pressures within the gas pockets are compared in detail below.

Figure 20 shows the pressure in these two regions at both scales. Time and Pressure at scale 1:6 have been Froude scaled.

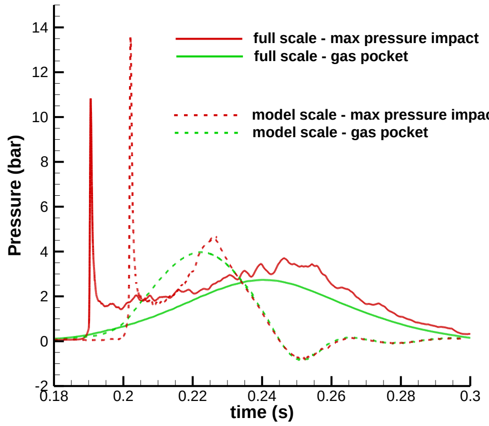

Figure 20 – Pressure time histories at location of max pressure and in the gas pocket for scale 1 (case 1) and scale 1/6 (case 2) calculations. *Time and pressure from Case 2 are Froude-scaled*.

A good qualitative similarity between the calculated results and experimental results from Sloshel as shown in **Figure 9** is obtained. The experimental recorded pressure signal for the sensor giving the maximal pressure is not as sharp as the calculated one, showing that this maximum was likely not captured with the density of pressure sensors available.

Table 2 gathers the main characteristics to be compared at both scales.

Table 2 - Main characteristics to be compared at both scales.

Case (scale)	P_{max} (bar)	$t(P_{max})$ (s)	P^{Pocket}_{max} (bar)	$t(P^{Pocket}_{max})$ (s)	$Period^{Pocket}$ (s)
1 (1:1)	10.8	0.1906	2.74	0.2402	0.23 - 0.25
2 (1:6)*	13.7	0.2021	3.96	0.0223	0.092

**Values at scale 1:6 have been Froude-scaled*

Froude-scaling the peak pressure and the gas pocket pressure from scale 1:6 to scale 1 leads to an overestimation of the actual full scale pressures. As already mentioned in the previous section, ***pressure peak obtained at scale 1:6*** is also delayed and ***frequency of the oscillations*** is higher.

Pressure inside the gas pocket (ELP3)

Maximum pressure within the gas pocket and period of the first oscillation are given in **Table 2** at both scales. The period is estimated as four times the duration of the pressure rise between 0 and P_{max}.

Bogaert et al. (2010) and Kimmoun et al. (2010) used successfully the 1D piston model of Bagnold to explain the scaling factors between pressures measured inside gas pockets entrapped by unidirectional breaking wave impacts on a vertical wall at two scales. The waves compared at two different scales had scaled initial water heights and scaled volumes of gas pocket. Lafeber et al. (2012b) used the same approach but with more accurately selected waves at both scales in order the inflow conditions could be considered as Froude-similar, before any gas compression during escaping phase started. The results matched well with Bagnold's theory. The same approach is followed with the two simulated waves at both scales.

Bagnold's problem can be written in dimensionless form. The solution only depends on one dimensionless number when the gas remains unchanged. The dimensionless number is called *Impact Number* and is defined by $S = \frac{\rho_0 L {v_0}^2}{P_0 x_0}$, where ρ_0, L, v_0, P_0, x_0 are respectively the liquid density, the liquid thickness (piston), the initial velocity of the piston, the initial pressure inside the gas chamber and the initial size of the chamber. **Figure 21** shows the dimensionless pressure $P^* = (P-P_0)/P_0$ versus the impact number S according to Bagnold's solution. The period of the oscillations can also be obtained simply as a function of S.

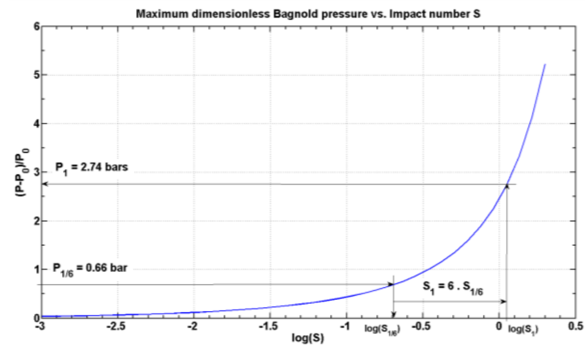

Figure 21 – Maximum dimensionless pressure vs. Impact number S, according to Bagnod's model of piston problem. Method to derive full scale gas pocket pressures from model scale's.

From the calculated maximum pressure within the gas pocket at scale 1:6 ($P_{1:6}$), can the associated impact number $S_{1:6}$ be derived on Bagnold's curve. When changing the scale under the assumption of Partial Froude Scaling, $S_{1:6}$ becomes S_1=6 $S_{1:6}$. The corresponding pressure at scale 1 (P_1) can then been obtained in the same way. When done for all pressures in the reasonable range at scale 1:6, the resulting curve allows the direct conversion of any pressure from scale 1:6 to scale 1, as far as air pocket pressure with water around at both scales are concerned. Same can be done easily for the periods.

Figure 22 shows this 'Bagnold' pressure converting curve together with the 'Froude' pressure converting curve from scale 1:6 to scale 1.

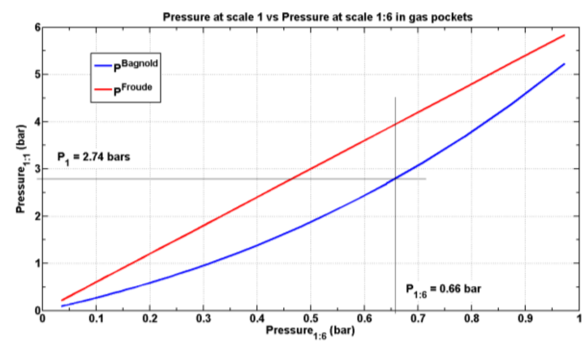

Figure 22 – Pressure at scale 1 vs. pressure at scale 1:6 for gas pockets. Derived from Bagnold's model of piston problem.

The pressures calculated at scale 1 (2.74 bars) and scale 1:6 (0.66 bar, this time without Froude-scaling) with respectively calculation Case 1 and Case 2 have been put directly on the two graphs. The two values are in perfect agreement with Bagnold's model. It is the same for the periods of oscillation, which is not shown here.

Pressure in the gas pocket is not much influenced by the deviation of the crest. The double oriented arrow in **Figure 2** between ELP2 and ELP3 should be corrected with only one single direction ELP3 → ELP2.

As, according to Lafeber et al. (2012b), Bagnold's model is relevant for scaling gas pocket pressures entrapped by real breaking waves, this result validates further *SPH-Flow* compressible bi-fluid version.

Pressure peak (ELP1, ELP2)

We have seen that the gas compressibility bias, namely the fact that gas at scale 1:6 ***is stiffer*** than at scale 1, induced ***crest trajectories*** slightly different at both scales. This led to a ***delayed impact***, at a slightly ***higher location*** at scale 1:6. Moreover the liquid flows initiated in the crest and splitting on both sides of the first contact point upwards and downwards along the wall had also their ***initial direction with regard to the wall*** slightly modified at scale 1:6. At the same time the ***horizontal velocity of the crest*** is smaller at scale 1:6 (9.1 m/s instead of 10.1 m/s). Consequently, it has been observed that the pressure surfaces P(y, t) had different characteristics at both scales in the area of the crest. With these already biased inflow conditions, trying to compare the resulting maximum pressures at both scales only by means of similarity laws is useless.

Nevertheless, it is worth observing that maximal pressure as calculated at scale 1:6 is 27% higher after Foude-scaling than when directly calculated at scale 1. This is to be considered as on the conservative side with regards to sloshing model tests.

In summary, it is not possible to compare the loads generated by the crest on the wall because there was an early interference of ELP3 before ELP1 and ELP2 come on stage (see first arrow between ELP3 and ELP1 in **Figure 1** and **Figure 2**). However it is numerically possible to suppress this interference by doing a restart calculation just before the first contact either for scale 1:6 calculation but after Froude-scaling all data (geometry, velocities and pressures) up to scale 1 or for scale 1 calculation but after Froude scaling all data down to scale 1:6. The first solution was chosen. The calculation case is referred to as Case 3 in **Table 1**. Now, the comparison is therefore to be made between Froude-scaled results of scale 1:6 calculation and restart calculation at scale 1 with Froude scaled input data.

Doing so, the influence of the gas compressibility bias, at least during the escaping phase, is supposed to be annihilated. Therefore only the liquid compressibility bias remains between the two calculations. If both calculations gave the same peak pressure, it would demonstrate clearly that liquid compressibility is not involved and would kill any claims of ELP1 on the load. In order to address this liquid compressibility potential bias more completely two other calculations were launched:

- Case 4 with the same conditions as Case 3 but with a Froude-scaled speed of sound in the liquid ($1500 * \sqrt{6} = 3674$ m/s). Doing so, conditions could be considered as close to CFS as far as just the crest impact is concerned. Therefore a perfect match between results of Case 4 and results of Case 2 after Froude scaling is expected.
- Case 5 with the same conditions as Case 3 or Case 4 but with a much smaller speed of sound in the liquid (343 m/s, namely the same as in the gas) in order to reduce as much as possible potential liquid compressibility influence.

Peak pressures for the four calculations (Case 2 to Case 5) are shown in **Figure 23**. No comparison is possible with Case 1 in these conditions.

The influence of the speed of sound in the liquid, therefore of the liquid compressibility on the maximum pressure is obvious. When keeping the same liquid compressibility at both scales (Case 2 and Case 3), maximum pressure is divided approximately by two. Maximum pressure increases when the liquid speed of sound increases. This seems to clearly indicate a large influence of ELP1. However, it should be kept in mind that the maximal pressure reached here (around 14 bars) is far from the maximum defined by the acoustic pressure with an impact velocity of 10 m/s, which would be 150 bars.

Pressures after the peak remain the same for all the restart calculations at scale 1, whatever the speed of sound in the liquid. It means that ELP1 has an insignificant influence on ELP3, which is not a surprise. The behavior of the gas pocket proved to be very stable. The double-oriented arrow between ELP1 and ELP3 in **Figure 2** should be drawn in only one direction: ELP3 → ELP1.

The fact that pressure in the gas pocket does not match when comparing Case 2 with any scale 1 restarted calculation is nothing new: it is due to the initial gas compressibility bias into the gas pocket.

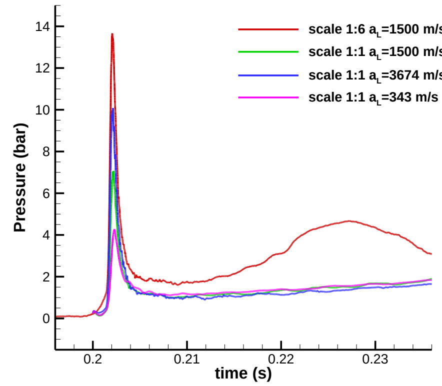

Figure 23 – Pressure time history at point giving the maximum pressure for Case 2 (red), Case 3 (green), Case 4 (blue), Case 5 (pink). Case 3, 4, 5 are restart calculations at scale 1 just before impact from Case 2 data after Froude-scaling.
Time and pressure from Case 2 are Froude-scaled.

However, even though results with Froude-scaled liquid speed of sound (Case 4) are closer to the reference Case 2 than when keeping the same speed of sound at both scales (Case 3), results could not be declared as a perfect match. Several explanations could be proposed as for instance a remaining compressibility bias during the fraction of time before the impact, as it was necessary to keep such a gap in order to ensure the first contact had not already occurred. Actually, it turned out that the discrepancy is due to a restart process which is not totally satisfying in the Software and leads to significantly smaller results when restarting the same calculation at a later time. The reason of this anomaly has been identified and should be corrected soon.

Therefore the reference calculation Case 2 had to be restarted ***at the same time*** before impact as the other cases (→ Case 2') for a fair comparison. All results are presented in **Figure 24**.

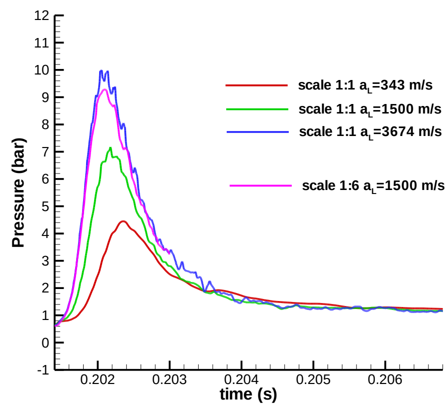

Figure 24 – Pressure time history at point giving the maximum pressure for Case 2' (pink), Case 3 (green), Case 4 (blue), Case 5 (red). Case 3, 4, 5 are restart calculations at scale 1 just before impact from Case 2 data after Froude-scaling. Case 2' is a restart from Case 2 at ***same time***. *Time and pressure from Case 2' are Froude-scaled*.

This time, a good match is obtained between Case 2' and Case 4. Because the compressibility bias of the gas has been annihilated and the compressibility of liquids are relevantly scaled, impact conditions for Case 2' and Case 4 can be considered as CFS and therefore the ***resulting pressures*** are the same.

By the way, this result also proves that, when already entrapped the compressibility of the pocket does not influence the peak pressure at the crest level. The double arrow in between ELP1 and ELP3 in **Figure 2** should finally completely be removed.

The interaction between ELP1 and ELP2 should also be addressed. **Figure 25** shows the pressure maps under view 1, restricted to the crest impact area, for the three restart calculations at scale 1, with therefore three different liquid speeds of sound.

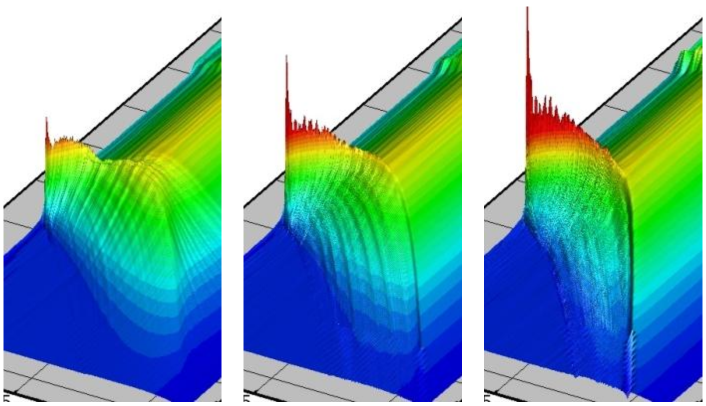

Case 5 C_L = 343 m/s *Case 3 C_L = 1500 m/s* *Case 4 C_L = 3674 m/s*

Figure 25 – Pressure maps in the crest area under View 1, for three different liquid speeds of sound.

Both area 1 and area 2 (see **Figure 15**) of the pressure surface P(y, t) are largely modified when the liquid speed of sound is changed. The sharp ridge that could intuitively be associated only to ELP2 at least after the transition with the peak would also have an ELP1 component, therefore associated to the liquid compressibility.

This point is to be addressed in detail in another study as it could be only a numerical artifact.

Actually a special study aiming at a better knowledge about ELP1, ELP2 and their interactions has been launched recently through numerical calculations. How far the structure is concerned by such high frequency-content pressure peaks is also an issue which should be addressed.

CONCLUSIONS

A unidirectional breaking wave impact on a rigid wall, involving the entrapment of a large air pocket, was simulated in 2D, at scale 1 and at scale 1:6, by means of two codes used sequentially. FSID, a potential code based on conformal mappings and a desingularized technique was used to initialize the computations of *SPH-Flow*, a SPH parallel solver of Euler equations for two compressible fluids. This initialization enables the SPH calculation to start just soon before the impact and save much computation time.

Same general characteristics of the wave shape and impact load as those observed by high speed cameras and recorded by pressure sensors during wave impact tests in flume tanks for such air-pocket type of impact, were captured by the simulations. This includes:

- the separation of the crest flow in two vertical jets upwards and downwards from the first contact point with the wall;
- The highly dynamic and localized pressure peak at this contact point (ELP1);
- The two pressure pulses travelling upwards and downwards with the roots of the jets (ELP2);
- The damped oscillations of the gas pocket (ELP3) and its extended influence on the wall loading below the pocket and within the crest.

Therefore, all local events that are at the origin of the Elementary Loading Processes are captured accurately by the numerical simulations.

Same scaling discrepancies with regard to Froude-scaling were found from simulations as from tests when comparing the last stage of the flow and the wall loading at scale 1 and at scale 1:6. These discrepancies are obviously due to the gas compressibility bias when the same gas is used at both scales. This includes the following general trends:

- The flow of escaping gas is stronger at the smaller scale;
- It generates a slight upwards deviation of the crest trajectory at scale 1:6, which leads to a higher location of the impact than at scale 1;
- Initial incidence of the crest flow with regards to the wall rotates also of a small angle upwards, which makes the upwards flow easier and the downwards flow more constrained after the separation around the contact point and modifies the strength of the travelling pressure pulses;
- Whatever the scale, pressure within the gas pocket evolves according to Bagnold's 1D model of gas compression by a piston. The small initial deviation of the crest at scale 1:6 due to the flow of escaping gas does not change significantly the trend: pressures in the gas pockets are Bagnold-similar at both scales.
- Therefore, maximal pressure in the gas pocket is higher at scale 1:6, if Froude-scaled, than at scale 1. Frequency of oscillations is higher at scale 1:6, after Froude-scaling, than at scale 1.

These good comparisons with experimental results bring credibility to the numerical simulations, at least with their ability to capture the relevant phenomena. But numerical simulations bring also many possibilities that experiments don't, including some virtual extensions of the reality. Some of them have already been used successfully:

- a high density of virtual pressure sensors was used along the wall during the simulations (1 sensor every 10 mm) in order to show an almost continuous time-space distribution of the load. This enabled to understand better how the different loading components combine at the wall.
- the biased compressibility effects of the escaping gas phase was annihilated for a more relevant study of the influence of liquid compressibility on the crest impact load, by simple restart calculations just before the impact.
- Liquid with virtual properties were used for the same objective.

These extended possibilities, compared to experiments, brought new insight on the wave impact loads:

- They showed a significant influence of the liquid compressibility not only on the magnitude of the very sharp pressure peak in the area of the first contact point, which was expected, but also on the magnitude of the travelling pressure pulse starting from this point, which was less expected. This last result must be further studied in order to verify whether it is an artifact or not.
- They enabled a more accurate vision on the interactions between the different ELPs that are so crucial for scaling.

After years of developments in order to fulfill the minimum requirements for a relevant simulation of liquid impacts, *SPH-Flow* is now ready for real applications and started to bring a kind of insight experiments could not bring. Many exciting possibilities are thus now offered, taking benefit of the continuous time and space distribution of the loads it provides and of the deterministic conditions easily generated for the crucial pending comparisons to be studied in the frame of sloshing in membrane LNG tanks:

- Impact on rigid wall compared to similar impact on any containment system (influence of hydro-elasticity);
- Impact on flat wall compared to similar impact with raised elements such as corrugations of Mark III and raised edges of NO96;
- Various Froude-similar inflow conditions for impacts to be studied at different scales.

GTT supports in parallel similar works on wave impact simulation but based on different numerical methods, such as finite volumes and finite elements. Only when these different methods give similar results for the same wave impact simulations, can the results be considered as completely reliable.

More generally, such numerical simulations, in addition to the development of sophisticated surrogate models (see Ancellin, 2012) or dedicated experiments (Lafeber et al., 2012) are performed in the frame of a research plan aiming at improving the sloshing model tests for a better experimental modeling of the reality (reduce the biases) and at defining a more direct scaling approach despite the remaining biases.

As the designer of the membrane containment systems for LNG tanks, the main objective of *GTT* remains the safety of its solutions onboard LNG carriers. Empirical scaling factors derived from the feedback at sea, namely from the knowledge that can be drawn from real sloshing incidents on board LNG carriers, still remains the safest scaling solution which is applied in the sloshing assessment of any new membrane LNG carrier.

ACKNOWLEDGEMENTS

HydrOcean, *GTT* and *ECN* acknowledge the computing resources offered by CCIPL, CRIHAN, and IFREMER.

The research leading to these results has received funding from the European Community's Seventh Framework Programme (FP7/2007-2013) under grant agreement #225967 "NextMuSE".

REFERENCES

Ancellin, M., Brosset, L., Ghidaglia, J.M., (2012), "*Influence of phase transition on sloshing impact pressures described by a generalized Bagnold's model*", 22th (2012) Int. Offshore and Polar Eng. Conf., Rhodos, Greece, ISOPE.

Bagnold, R., (1939), *"Interim report on wave-pressure research"*, J. Inst. Civil Eng. 12: 201–226.

Bogaert, H., Brosset, L., Léonard, S., Kaminski, M., (2010), *"Sloshing and scaling: results from Sloshel project"*, 20th (2010) Int. Offshore and Polar Eng. Conf., Beijing, China, ISOPE.

Braeunig, J.-P., Brosset, L., Dias, F., Ghidaglia, (2009), "*Phenomenological study of liquid impacts through 2D compressible two-fluid numerical simulations*", 19th (2009) Int. Offshore and Polar Eng. Conf., Osaka, Japan, ISOPE.

Brosset, L., Lafeber, W., Bogaert, H., Marhem, M., Carden, P., Maguire, J., (2011), "*A Mark III Panel Subjected to a Flip-through Wave Impact: Results from the Sloshel Project*", 21st (2011) Int. Offshore and Polar Eng. Conf., Maui, (HI), USA, ISOPE.

Deuff, J.-B., (2007), *"Extrapolation au réel des mesures de pressions obtenues sur des cuves modèle réduit"*, PhD Thesis, Ecole Centrale de Nantes/*GTT*, France.

Doring, M., (2005). *"Développement d'une méthode SPH pour les applications à surface libre en hydrodynamique"*, PhD Thesis, Ecole Centrale de Nantes, France.

Drazin, P.G., Reid, W.H., "*Hydrodynamic Stability*", Cambridge University Press, 2004

Gervaise, E., de Sèze, P.E., Maillard, S., (2009) *"Reliability-based methodology for sloshing assessment of membrane LNG vessels"*, 19th (2009) Int. Offshore and Polar Eng. Conf., Osaka, Japan, ISOPE.

Grenier, N., (2009). *"Modélisation numérique par la méthode SPH de la séparation eau-huile dans les séparateurs gravitaires"*, PhD Thesis, Ecole Centrale de Nantes, France.

Guilcher, P.-M., (2008). *"Contribution au développement d'une méthode SPH pour la simulation numérique des interactions houle-structure"*, PhD Thesis, Ecole Centrale de Nantes, France.

Guilcher, P.-M. , Oger, G., Brosset, L., Jacquin, E., Grenier, N. and Le Touzé, D., (2010) "*Simulations of liquid impacts with a two-phase parallel SPH model*", Proceedings of 20th (2010) Int. Off. And Polar Eng. Conf., Beijing, China.

Kaminski, M.L., Bogaert, H., Brosset, L., (2011). "*Full and large scale wave impact tests for a better understanding of sloshing – Results of the Sloshel project*", 30th (2011) Int. Conf. on Ocean, Offshore and Arctic Eng. OMAE 2011-49992, Rotterdam, the Netherlands.

Kaminski, M.L., Bogaert, H., (2010). "*Full-Scale Sloshing Impact Tests Part II*", 20th (2010) Int. Offshore and Polar Eng. Conf., Beijing, China, ISOPE.

Lafeber, W., Brosset, L., Bogaert, (2012a) "*Elementary Loading Processes (ELP) involved in breaking wave impacts: findings from the Sloshel project*", 22th (2012) Int. Offshore and Polar Eng. Conf., Rhodos, Greece, ISOPE.

Lafeber, W., Brosset, L., Bogaert, (2012b), "*Comparison of wave impact tests at large and full scale: results from the Sloshel project*", 22th (2012) Int. Offshore and Polar Eng. Conf., Rhodos, Greece, ISOPE.

Leduc, J., Marongiu, J.-C., Leboeuf, F., Parkinson, E., (2009) *"Multiphase SPH: A new model based on Acoustic Riemann solver"*, Proc. Of the 4th Spheric Workshop (2009), Nantes, France.

de Leffe, M., (2011). *"Modélisation d'écoulements visqueux par méthode SPH en vue d'application à l'hydrodynamique navale"*, PhD Thesis, Ecole Centrale de Nantes, France.

Oger, G., (2006). *"Aspects théoriques de la méthode SPH et applications à l'hydrodynamique à surface libre"*, PhD Thesis, Ecole Centrale de Nantes, France.

Oger, G., Brosset, L., Guilcher, P.-M., Jacquin, E., Deuff, J.-B. and Le Touzé, D., (2009) "*Simulations of hydro-elastic impacts using a parallel SPH model*", 19th (2009) Int. Offshore and Polar Eng. Conf., Osaka, Japan, ISOPE.

Scolan, Y.-M., (2010) *"Some aspects of the flip-through phenomenon: A numerical study based on the desingularized technique"*, Journal of Fluids and Struct. 26, 918-953.

Swegle, J. W., Hicks D. L., Attaway S. W., (1995). "*Smoothed particle hydrodynamics stability analysis*", Comput. Methods. Appl. Mech. Eng., 116, 123-134.

Vila, J.P., (2005) *"SPH Renormalized Hybrid Methods for Conservation Laws: Applications to Free Surface Flows",* Meshfree Methods for Partial Differential Equations II, 43 (2005).

Vila, J.P., (1999) *"On Particle Weighted Methods and Smooth Particle Hydrodynamics",* Mathematical Models and Methods in Applied Sciences (1999).